Effect of self-mixing polarization on DFB laser diode chaotic dynamics

H. KHALAF[1,2], A. HEMED[1,*]
[1]*Department of Physics, College of Education, Mustansiriyah University, Baghdad - Iraq*
[2]*College of Remote Sensing and Geophysics, Alkarkh University of Science, Baghdad – Iraq*

In this simulation study, two identical laser devices are considered as if they represent a single laser device; the intent is to overcome limitations in simulation software, OptiSystem 21. Operating parameters for these two devices are selected to be the same. The study simulated the self-mixing nonlinear effect by optical feedback via single-mode optical fiber by following the Lang-Kobayashi model. Results for observed spectroscopy related to laser dynamics during self-mixing are included for large-scale fiber lengths (5, 10, and 15 km); this is to be able to employ sensing in harsh environments. Variations in signal parameters included polarization degree and state, which in practice arise with fiber bend and twist, resulting in birefringence and subsequently different group delay. They are considered in the experiment to control chaotic dynamics. Results confirmed effectiveness for suggested signal parameter variations by giving rise to laser dynamical chaoticity specifications. Calculated Correlation Dimension is fluctuated from 2.8158 to 3.1564 which approves the chaoticity for results. Accordingly, the observed spectrum bandwidth was changed to be 10 GHz with a fiber length of 5 km and 45° of polarization. The increase in chaotic signal bandwidth (BW) was reduced to 8.6 GHz at a 10 km optical fiber length and 0° polarization. As for 15 km, the bandwidth reached 8.6 GHz at -90° of polarization. These variations in laser spectrometry indicated more efficient sensors based on the high sensitivity property of chaotic dynamics. Such a novel sensor needs less complicated interferometry.

(Received December 3, 2025; accepted April 8, 2026)

Keywords: Polarization, Birefringence, Chaoticity, Laser diode, Self-mixing

1. Introduction

Laser chaos presents significant applications in many fields, including cryptographic secure communications, neural networks [1], distributed optical fiber sensing, random number generation, and chaotic laser radar [2, 3, 4, 5, 6]. Due to their complex dynamic characteristics and rapid responsiveness, laser diodes (LDs) are frequently used as chaotic light sources. However, due to relaxation oscillation frequency (ROF) limitations, the chaotic signal generated by LDs generally demonstrates the limitation of restricted bandwidth [7]. Many solutions have been developed to enhance chaotic bandwidth and address the issue of employing encryption [8], to gain extra bandwidth. For example, a study by Schires K. et al. [9] looked at the chaotic behavior of a distributed feedback laser (DFBL) when it had both short and long feedback. The results show that the chaotic bandwidth could go above 16 GHz when a hybrid III-V/Si DFBL with an ROF of 14 GHz is used. Xuejie Mu et al. [10] theoretically and experimentally generated broadband chaos over 24 GHz is available by developing a self-mixing laser system via optical feedback frequency modulation. The system is beneficial for high-speed broadband communication and sensing applications. Chai M. et al. [11] showed that adding an optical feedback loop to a chaotic LD chip causes nonlinear frequency mixing within the cavity. This causes the chaos bandwidth to grow to 33.6 GHz, which is 4.4 times more than the bandwidth without optical feedback (OFB). Hong Han et al. [12] performed a theoretical investigation on enhancing chaotic bandwidth in Fabry-Pérot LDs utilizing single-mode and dual-mode optical injection of DFB. The results indicate that the chaotic bandwidth may exceed 35 GHz with dual-mode optical infusion, which is six times larger than that observed without optical injection. Chaos is typically generated with bandwidths of several GHz using LDs with OFB, optoelectronic feedback (OEFB), and optical injection (OI) [13]. OEFB occurs via electric devices such as amplifiers and/or attenuators. Yet, OFB in LD is executed by re-injecting certain amounts of the laser emission output using a ring cavity, using optical fiber, or via free space configurations [14, 15, 16]. Recently, OI and OFB have been utilized to achieve unidirectional coupling in injected LDs [17].

Polarization chaos, a novel form of optical chaos, has been established. The essential physical mechanism of this polarization chaos is a nonlinear interaction between two elliptically polarized modes via birefringence (B) in optical fibers, generated intentionally [18]. A technique for creating bandwidth-enhanced chaos with a polarization controller (PC) is proposed, emphasizing the advantages

of polarization chaos. The PC is a piece of equipment that enables the adjustment of the polarization state of light. PC is employed to convert polarized or unpolarized light into an exact SOP. PC in free space transmitted signal often consists of rotating retarders (wave plates), it can be classified based on two rotating quarter-wave plates, two switched quarter-wave plates with one rotated half-wave plate, or one rotated quarter-wave plate matched with one rotated half-wave plate [19]. When the PC is set at the right orientation, the chaotic fiber laser reveals a period-doubling route to chaos [20].

It has been observed that the wide bandwidth provided by optical fibers cannot be fully utilized. The main factor contributing to the issue is polarization mode dispersion (PMD). PMD is a critical constraint that prevents optical fiber communication systems from optimizing their bandwidth. Unpredictable fluctuations in the B of an optical fiber induce PMD. The difference in differential group delay (DGD) between the two main principal states of polarization (PSP) in the optical fiber can be used to describe PMD [21].

2. Theoretical analysis

The refractive index of an optical fiber governs the velocity at which optical pulses traverse it. In a perfectly symmetrical optical fiber, the polarization of the light shouldn't change the speed of the light moving along the fiber because light has the same refractive indices, whether it is polarized along the X or Y axis [22]. In the single-mode fiber phase, the velocities of two orthogonal modes in the fiber $v_{f,x}$ and $v_{f,y}$ are defined by the values of the respective modes' wave numbers β_x and β_y [18]:

$$v_{f,x} = \frac{2\pi f}{\beta_x} \tag{1}$$

$$v_{f,y} = \frac{2\pi f}{\beta_y} \tag{2}$$

where f is the frequency of the traveling wave.

When the refractive indices in the X and Y directions vary due to any perturbation altering the fiber's influence, this variance is defined earlier as B. Because optical fiber is a birefringent medium, the SOP that oscillates along the "slow axis," which has a higher refractive index, propagates more slowly than the SOP that oscillates along the "fast axis," which has a lower refractive index. The net consequence of this B in the fiber induces a delay between two SOPs. This delay produces DGD, and the DGD per unit length is designated as PMD. The wave's general polarization state is elliptical, while in particular, two available cases are circular and linear Bs.

It is impossible to call one mode "fast" and the other "slow" when a wave with linear polarization goes through a birefringent fiber whose core cross-section changes slowly over time. The mode phase shift controls the output polarization state $\Delta\phi$, which is based on the average wave number range and the fibre length [23, 24, 25]:

$$\Delta\phi = \left(\overline{\beta_x} - \overline{\beta_y}\right) l_b \tag{3}$$

$$l_b = \frac{2\pi}{\beta_x - \beta_y} = \frac{\lambda}{n_{x,eff} - n_{y,eff}} = \frac{\lambda}{\Delta n_{eff}} \tag{4}$$

where; l_b is the fiber beat length, and the effective refractive indices in the X and Y axes are represented by $n_{x,eff}$ and $n_{y,eff}$. Δn_{eff} is the difference between effective refractive indices and λ is the light wavelength.

Polarization instability may induce chaos in the output polarization state if the linear B of a fiber varies throughout its length. This may happen if the fiber is regularly twisted throughout the spinning process onto a drum. Periodically rocking the preform or applying a periodic stress distribution can introduce modulated B during fiber manufacture. The twisting of birefringent fibers creates two simultaneous effects. The first axis is no longer stationary but rotates periodically along the fiber length. The second is that shear strain generates circular B under the twist rate. When both of these effects are included, then the birefringence can be described by the following equations [26]:

$$\frac{dA_+}{dz} = ib_c A_+ + \frac{i\Delta\beta}{2} e^{2ir_t z} A_- + \frac{2i\gamma}{3}(|A_+|^2 + 2|A_-|^2)A_+ \tag{5}$$

$$\frac{dA_-}{dz} = ib_c A_- + \frac{i\Delta\beta}{2} e^{-2ir_t z} A_+ + \frac{2i\gamma}{3}(|A_-|^2 + 2|A_+|^2)A_- \tag{6}$$

where A_+ and A_- illustrate right- and left-handed circular polarization, such that:

$$A_+ = \frac{\bar{A}_x + i\bar{A}_y}{\sqrt{2}} \tag{7}$$

$$b_c = \frac{hr_t}{2\bar{n}} \tag{8}$$

and b_c is related to circular birefringence, r_t is the twist rate per unit length, $\bar{n}$ and is the average mode index, the parameter h has a value of ~0.15 for silica fibers.

The equations initially derived by Lang and Kobayashi can be used to do a thorough study of the LD with OFB [27]. It is noted that the back-reflected light interferes with the light that is already in the cavity via self-mixing, which is a summary of the consequences of the optical delayed feedback. The LD threshold condition is adjusted based on the delay and the phase of the

reflected light; as a result, the emitted power varies while the pump current remains constant. The wavelength of the light emitted by the LD, which is subject to back reflections, is also somewhat altered due to the change in the threshold, indicating a variation in the actual LD carrier density [28]. The characteristic timescale of the self-mixing effect is comparable to the carrier LD lifespan, meaning it falls within the sub-nanosecond range, because it involves a change in carrier density [29].

Finding an analytical steady-state solution that is useful for sensing applications is simple and yields the general formula for the power released by the LD as follows [30]:

$$P(\emptyset) = P_0[1 + mF(\emptyset)] \tag{9}$$

where P_0 is the power emitted by the unperturbed LD, m is the modulation index and $F(\emptyset)$ is a periodic function of the interferometric phase $\emptyset = 2ks$, of period 2π. The modulation index m and the shape of the function $F(\emptyset)$ depend on the so-called feedback parameter C:

$$C = \frac{ks\sqrt{1+\alpha^2}}{L_{las}n_{las}} \tag{10}$$

where L_{las} is the LD cavity length, α is the LD linewidth enhancement factor, n_{las} is the cavity refractive index, and κ is given by: $k = \frac{\varepsilon}{\sqrt{A}}\frac{1-R_2}{\sqrt{R_2}}$, where A is the total optical power attenuation in the external cavity, and $\varepsilon \leq 1$ accounts for a mismatch between the reflected and the lasing modes, and R_2 is the LD output facet power reflectivity. Thus, the value of the C parameter depends on both the feedback amount and the important parameter, which is the "target distance" s.

The C parameter plays an important role because it uses the following inequalities to differentiate between various feedback regimes [29]:

$$\left.\begin{array}{c} C \ll 1 \rightarrow very\ weak\ OFB \\ 0.1 < C < 1 \rightarrow weak\ OFB \\ 1 < C < 4.6 \rightarrow moderate\ OFB \\ C > 4.6 \rightarrow strong\ OFB \end{array}\right\} \tag{11}$$

Analytical calculations given by the last Ref. showed that each OFB level has characterized LD signals as: cosine, non-symmetrical, sawtooth-like (bi-stability and hysteresis), and mode-hopping regime, respectively. Recording that in the last regime, interferometric measurements are not possible anymore.

In this experiment, self-mixed polarization within incoherent OFB will be used to make the chaotic behavior of a single-longitudinal-mode DFBL more robust. The Analysis of the LD system linewidth will be conducted using time series data collected from a mixed storage oscilloscope (MSO), radio-frequency (RF) data obtained from an RF spectrum analyzer, and optical spectrum analysis.

3. Simulation set-up

Fig. 1 shows the simulation setup for enhancing bandwidth in optical chaos using OptiSystem 21 software. Although the experiment simulates the self-mixing effect, the figure illustrates two twin (identical) DFBL devices that are similar in all operating parameters, in addition to the device model in software. Duplication is to overcome the limitations presented in the Optisystem 21 software when subjecting LD to self-mixing. A portion of the optical signal generated by the first laser is directed to an optical spectrum analyzer (OSA) and an optical power meter to measure the free-running optical power. The optical signal for the first DFBL is sent to the PC, then the PMD emulator, which consists of two instruments that modify the state of polarization (SOP), and then it introduces B. This, in turn, generates a DGD that affects the PMD. This adjusted signal is sent to the second DFBL through its simulated optical input port. RF signal for both is being investigated using an RF spectrum analyser via two avalanche photodetectors (APDs). MSO, eye diagram, and polarization analyzer are all used to observe the output oscillations. Free-running laser dynamics is initially observed to operate at a constant wavelength of λ = 1550 nm and a virtual laboratory temperature of T = 25° C. The Poincaré sphere can be recognized using a polarization analyser directly, which is connected to the PMD.

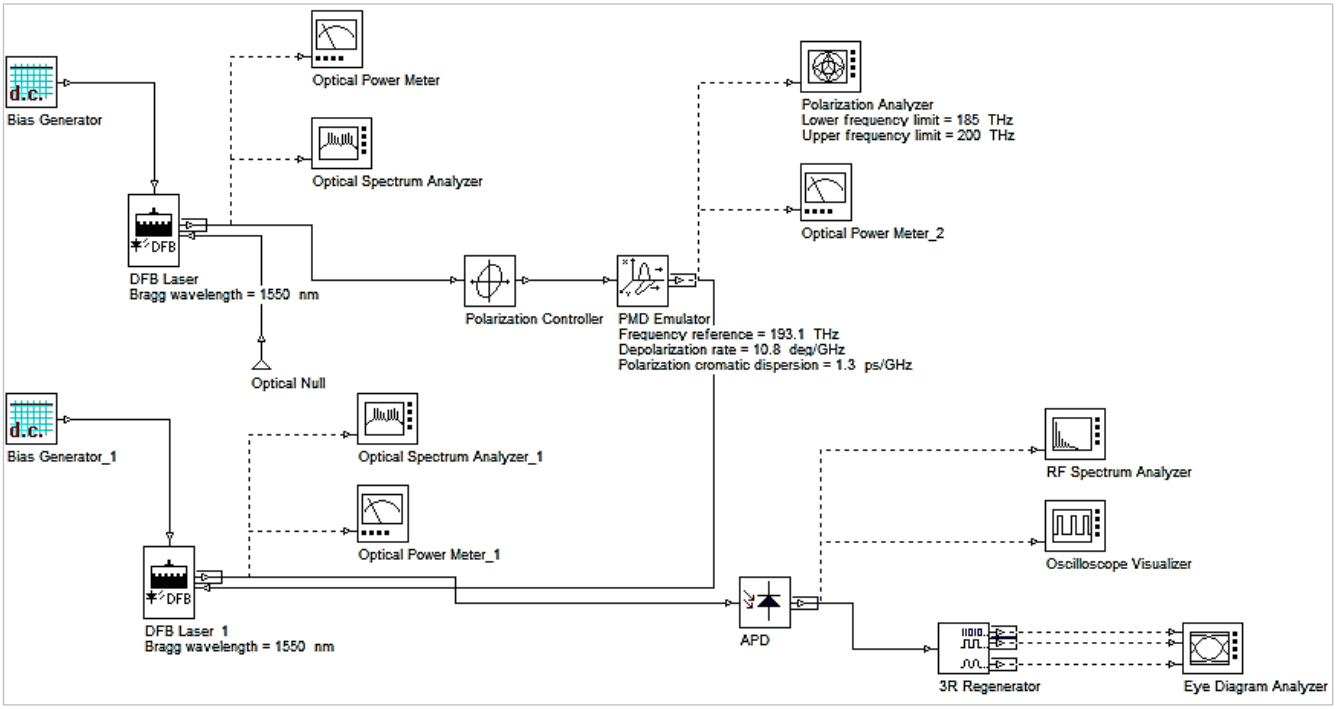

Fig. 1. Configuration set-up for chaotic dynamics with self-mixing (colour online)

4. Results and discussion

Firstly, spectroscopy and characteristics of the free-running DFB, such as the light-current (L-I) curve, are investigated. Fig. 2 (A, B, C, D) shows free-running DFB laser dynamics considering optical (OSA), radio frequency (RF), time series, and phase space spectra, respectively. This will be compared to the same laser behavior after including the self-mixing with the effect of twisting or bending-induced polarization. This is done by changing the optical fiber's medium polarization state and length. According to the OSA spectrum, the laser has an extended and broadened spectrum from 1.54995337 to 1.55001157 um, identical to the frequency period of 0.0252807439 to 5.7913970804966 GHz, with peak power amplitudes of 15.206625758668 uW and 35.36941580756 nW for the two observations, respectively. Fig. 2 shows the L-I curve of the solitary DFB laser at a temperature of 25° C, the figure-based threshold current is 17 mA, and λ=1550 nm. Above the threshold current, the optical output power demonstrates a nearly linear increase relative to the input current before reaching the saturation region. The last calculation is important for the determination of the laser bias level during the simulation.

Characterizing the ellipticity of the radiation emitted is not enough to determine the sample's birefringence parameters. To do this, different analytical and graphical methods have been created, such as those reported in ref. [31], which focuses on how polarization changes in various situations. Graphical tools provide clarity, especially in complicated scenarios. After watching how the free-running DFB behaved, the polarization state altered at several angles and for three different lengths of optical fiber. The PMD emulator, located just after the polarization control component, is also used to demonstrate signal distortion caused by PMD effects, as illustrated in Fig. 1. The system simulates a data rate of 10 Gb/s. The Poincaré sphere has been utilized to determine the state of polarization (SOP).

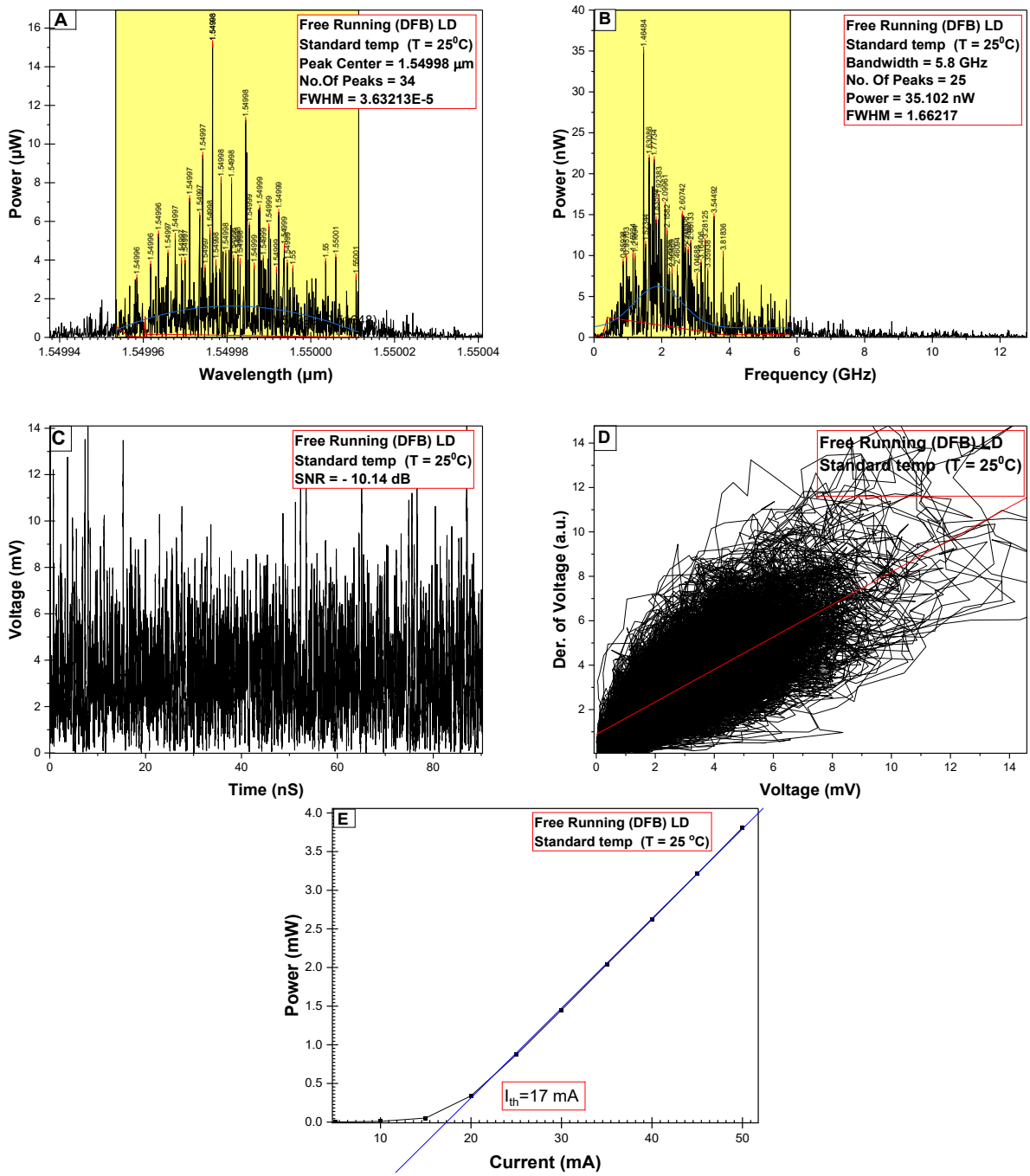

Fig. 2. Spectroscopy for free-running DFB laser. (A) Optical Spectrum Analyzer spectrum, (B) The Radio Frequency (RF) spectrum, (C) Time series, (D) Attractor, (E) L-I curve (colour online)

Fig. 3 illustrates the Poincaré SOP graph under the selected values for ellipticity and azimuth angle. Selection for these values was based on observed dynamics for the experiment. Each polarization can be seen as a point on the sphere (for entirely or partially polarized light) in a rectangular coordinate system. The centre of the Poincaré sphere indicates unpolarized light. The coordinates of the spot represent normalized Stokes parameters. All linear SOPs are situated along the equator. The right circular SOP sits at the north pole, while the left is at the south pole. Elliptically polarized states are shown across the entire surface of the Poincaré sphere. The two orthogonal polarizations are positioned as opposed to the sphere.

Ref. [19] reports that the continuous development of SOP manifests as a constant trajectory, and then the phase shift causes the initial SOP to shift to a new SOP along the same line. The blue line in the Poincaré sphere shows the first Stokes parameter S1(1,0,0) for horizontally linearly polarized light (HLP) and S1(-1,0,0) for vertically linearly polarized light (VLP), indicating the difference in intensities between HLP and VLP.

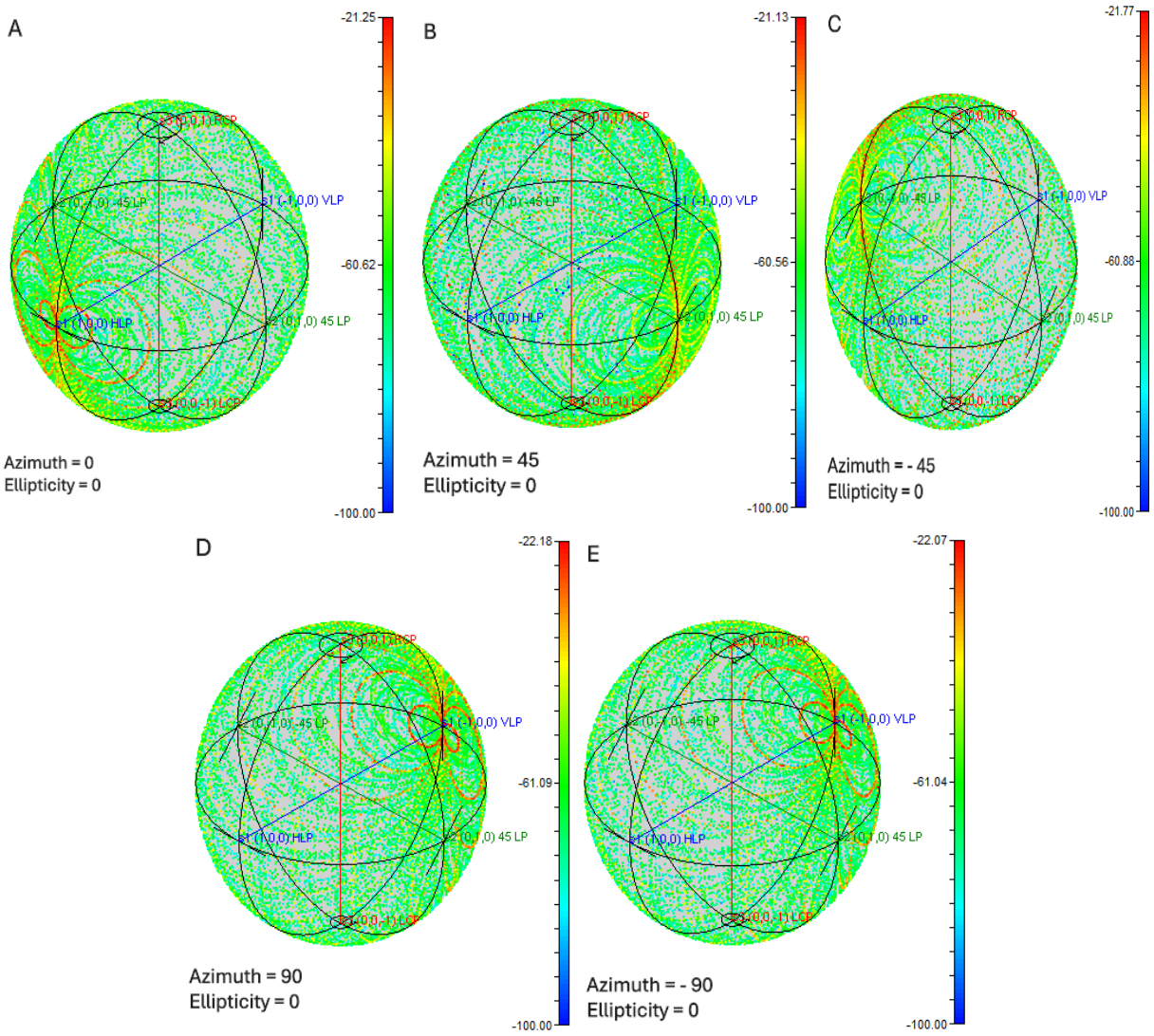

Fig. 3. Observed polarization fluctuations in the carried signal according to the sphere of Poincaré. (A) The azimuth is 0°, and the ellipticity is 0°, (B) The azimuth is 45°, and the ellipticity is 0°, (C) The azimuth is -45°, and the ellipticity is 0°, (D) The azimuth is 90°, and the ellipticity is 0°, and (E) the azimuth is -90° and the ellipticity remains 0° (colour online)

In contrast, the green line represents linear polarization (LP) and links the Stokes parameters S2 (0,1,0) at 45 LP and S2 (0, -1,0) at -45 LP. The red line on the sphere exhibits the third Stokes parameter, S3(0,0,1), for right circularly polarized light (RCP) and S3(0, 0, -1) for left circularly polarized light (LCP), demonstrating the difference in their intensity.

Fig. 3 also shows that the points will be spread out in an elliptical pattern on the sphere's surface when the two principal polarization states (azimuth and ellipticity) change. This is because a higher DGD value makes the points spread out in an elliptical shape; however, a lower DGD value makes the points spread out evenly across a sphere [32]. After the change in birefringence and the appearance of the DGD, along with an analysis of the signal from the PMD through the Poincaré sphere, the next section looks at how these changes affect the formation of a chaotic system for the laser feedback signal. The outcomes of this signal will be further analysed when it interacts with the laser device's active medium via self-mixing. This is according to observations of optical spectrum analyser, RF analyser, and MSO against three different lengths of optical fiber (5 km, 10 km, 15 km).

Chaotic systems are often defined by irregular, aperiodic behaviour that seems random yet is deterministically governed by underlying factors. The time series of chaotic oscillations can exhibit very unpredictable and irregular patterns. In chaotic oscillation time series, the relationship between voltage and time comprises complicated, unexpected patterns, dynamics that aren't linear, attractors, bifurcations, Lyapunov exponents, fractal structures, and new phenomena that appear out of nowhere. Each variable enhances the complexities and unpredictability of voltage oscillations in chaotic systems.

Fig. 4 illustrates the simulation accomplished utilizing the principal polarization states (azimuth = 0° and ellipticity = 0°) for a PMD simulator with a fibre length of 5 km. Compared to the free-running DFB situation, Fig. 2, the OSA results indicate a change in the central wavelength and an increase in peak power to attain a value of P = 48 µW. Reduction in dynamics was observed, according to calibration, for resulting spikes of only 5 peaks, as shown in part A of this figure. In contrast, Fig. 4B shows the RF analysis, which indicates that the chaotic BW has extended to 8.8 GHz, and the number of spikes has doubled compared to the free-running situation. Additionally, the dynamics showed increased power for the spikes, with the highest mode reaching 27 nW.

Fig. 4C demonstrates the system's voltage variations as it progresses according to its essential dynamics. By evaluating the signal-to-noise ratio (SNR), one can analyze and quantify the influence of self-mixing chaos on the resultant signal in terms of estimated noise. The SNR is found by dividing the power of the signal by the power of the noise [33]. The results for the free-running DFB showed that the SNR value is -10.14 dB, which fluctuated slightly for the dynamic readings resulting from each change in polarization state.

Acceptance and understanding of the future behaviour of chaotic systems demand an analysis of attractor observation. The system evolves toward an attractor, which includes a set of states, irrespective of the original conditions. It signifies the prospective condition of the system's behaviour. Fig. 4D illustrates the attractor for the chaotic system by altering SOP. This behaviour is characterized as a strange attractor, a type of attractor arising from chaotic system dynamics. Assume that the strange attractor exhibits chaos and is very sensitive to initial conditions. So, after a certain number of iterations, any two different initial points on the attractor that are infinitesimally close will eventually come together to form points that are also infinitesimally close. After the same number of iterations, they will separate to form points that are arbitrarily far apart (within the boundaries of the attractor). A dynamic system with a chaotic attractor is locally unstable yet globally stable. Following particular sequences that converge on the attractor, adjacent points separate from one another yet remain within the area around them [34].

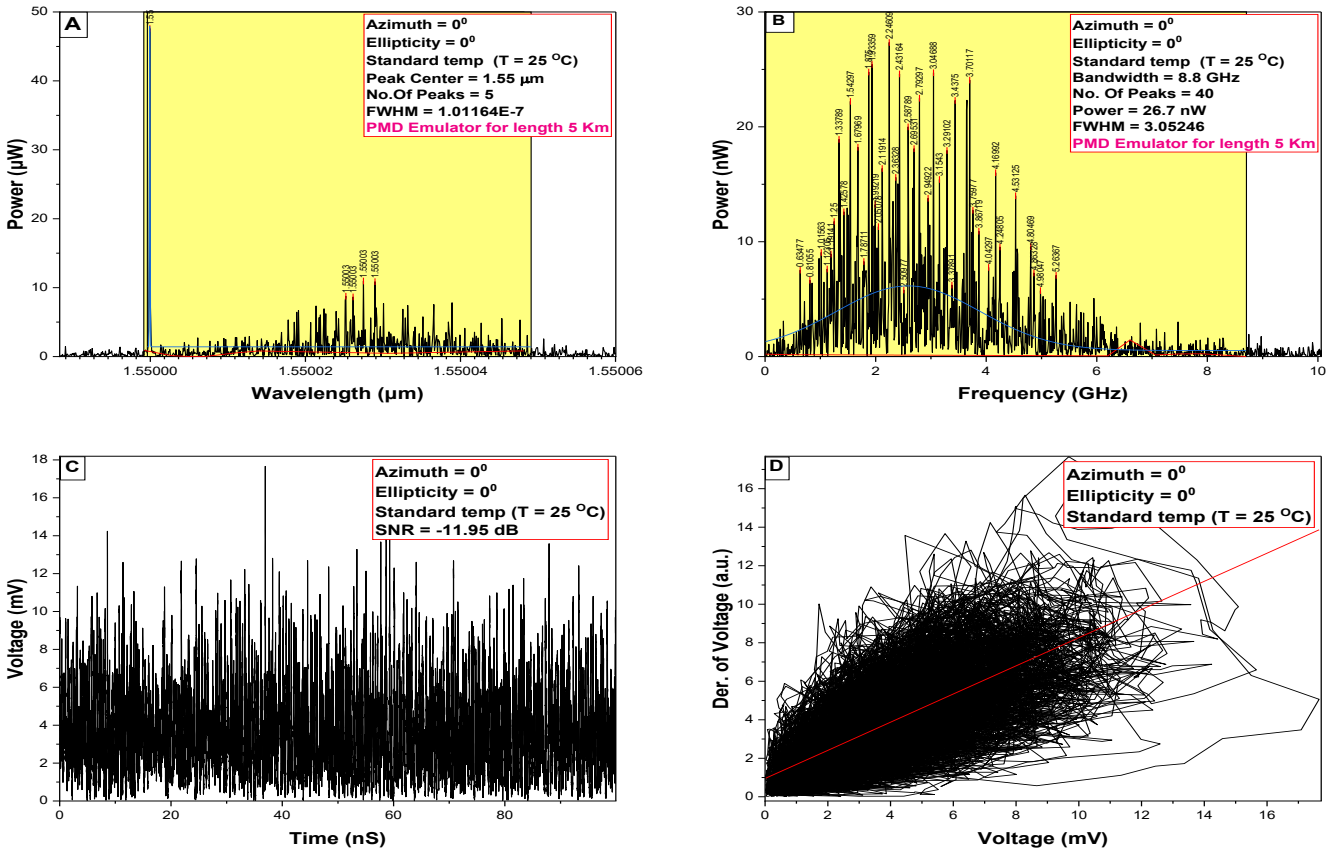

Fig. 4. Signal analysis after applying azimuth = 0° and ellipticity = 0, L = 5 km. (A) Optical Spectrum, (B) The RF power spectra, (C) Time series, (D) The attractor (colour online)

Fig. 5 reveals a notable improvement compared to Fig. 4. When the two main polarization states were changed to (azimuth = 45° and ellipticity = 0°), it was seen in Fig. 5A that the OSA had a changed in the central wavelength and the chaotic dynamic range grew compared to the previous case (Fig. 4A). Fig. 5B illustrates an increase in BW, which reached 10 GHz, and convergence in the number of peaks. Fig. 5C shows a slight decrease in

the frequency intensity, approximately 736 peaks compared to the free-running case, which is approximately 848 peaks. Fig. 5D verifies that the signal maintains its periodicity, and the measured slope is found to be 0.72, which is slightly less than the case of free-running, where the slope value was 0.73. SOP modification creates birefringence and, hence, the appearance of DGD. The value of DGD can be weak, moderate, or high. Fig. 5 shows that the DGD rating is moderate, where it is proportional to an increase in the chaotic bandwidth and intensity fluctuations in the time domain.

Upon the alteration of the azimuth angle in the reverse direction (azimuth = -45° and ellipticity = 0°), a sequence of modifications in the chaotic dynamics is seen, as illustrated in Fig. 6A the OSA demonstrates a consistent shift in the center wavelength, as shown in the preceding figures. Still, the dynamics retain the same behavior previously exhibited at an azimuth angle of 45° regarding the frequency peak numbers. Notably, there is a reduction in BW relative to the earlier case when the azimuth was 45°, along with a slight decrease in the center frequency power (P = 19.88 nW) as shown in (Fig. 6B). The analysis of the time series of chaotic oscillations reveals a progressive increase, with the frequency peaks attaining a value of 827, indicating an increment of 1.1%. The attractor statistics confirm a reduction in the slope value, which continues to decline as experienced in the two preceding cases, ultimately reaching 0.69, so verifying the continual alteration in the chaotic dynamics, Fig. 6C & D.

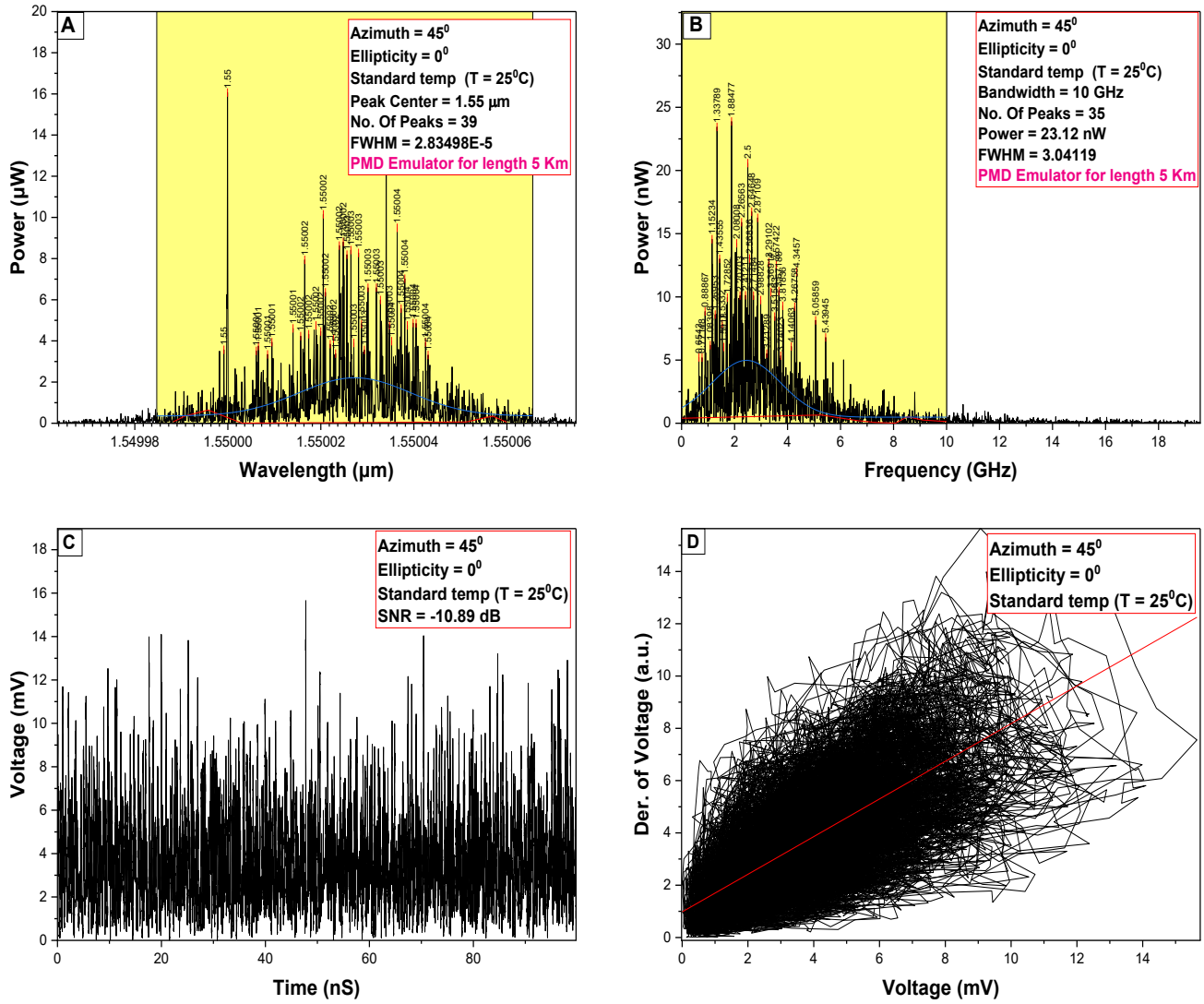

Fig. 5. Signal analysis after applying azimuth = 45° and ellipticity = 0°, L = 5 km. (A) Optical Spectrum, (B) The RF power spectra, (C) Time series, (D) The attractor (colour online)

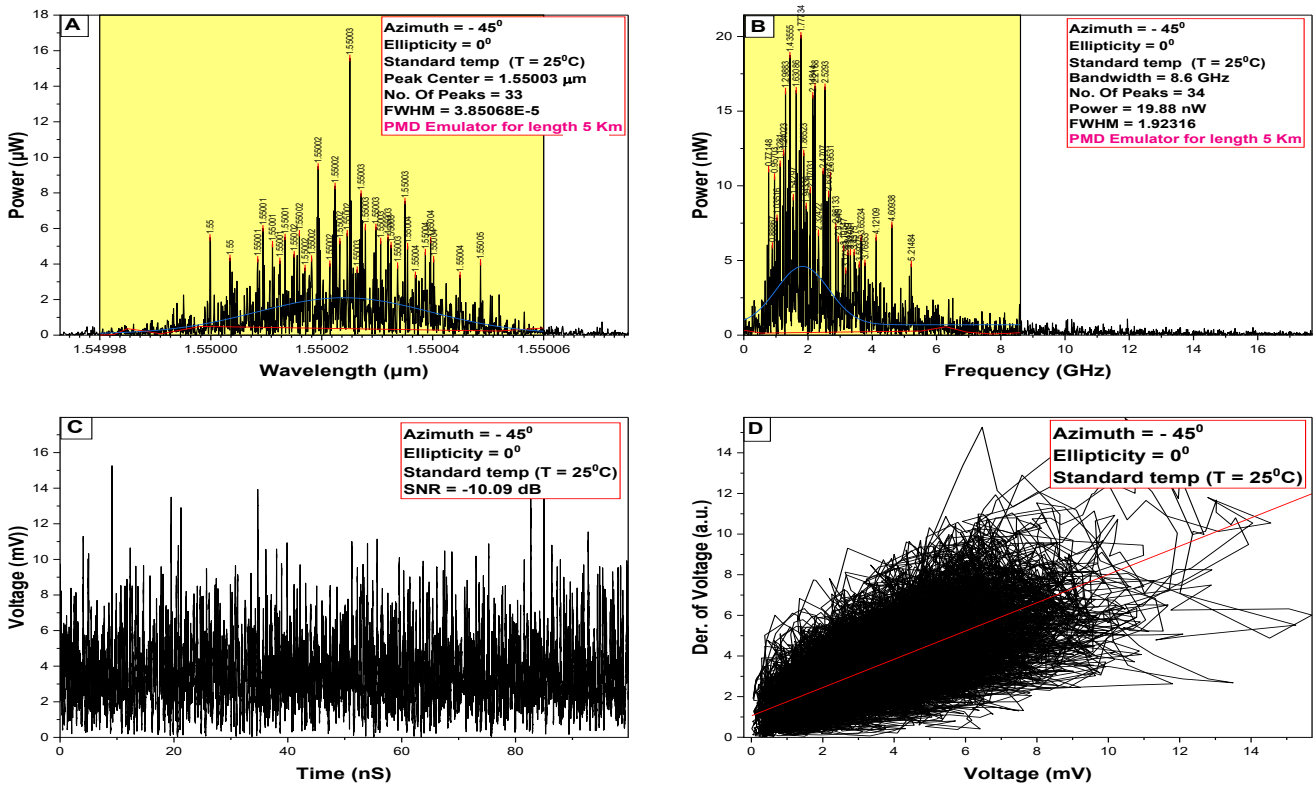

Fig. 6. Signal analysis after applying azimuth = -45° and ellipticity = 0°, L = 5 km. (A) Optical Spectrum, (B) The RF power spectra, (C) Time series, (D) The attractor (colour online)

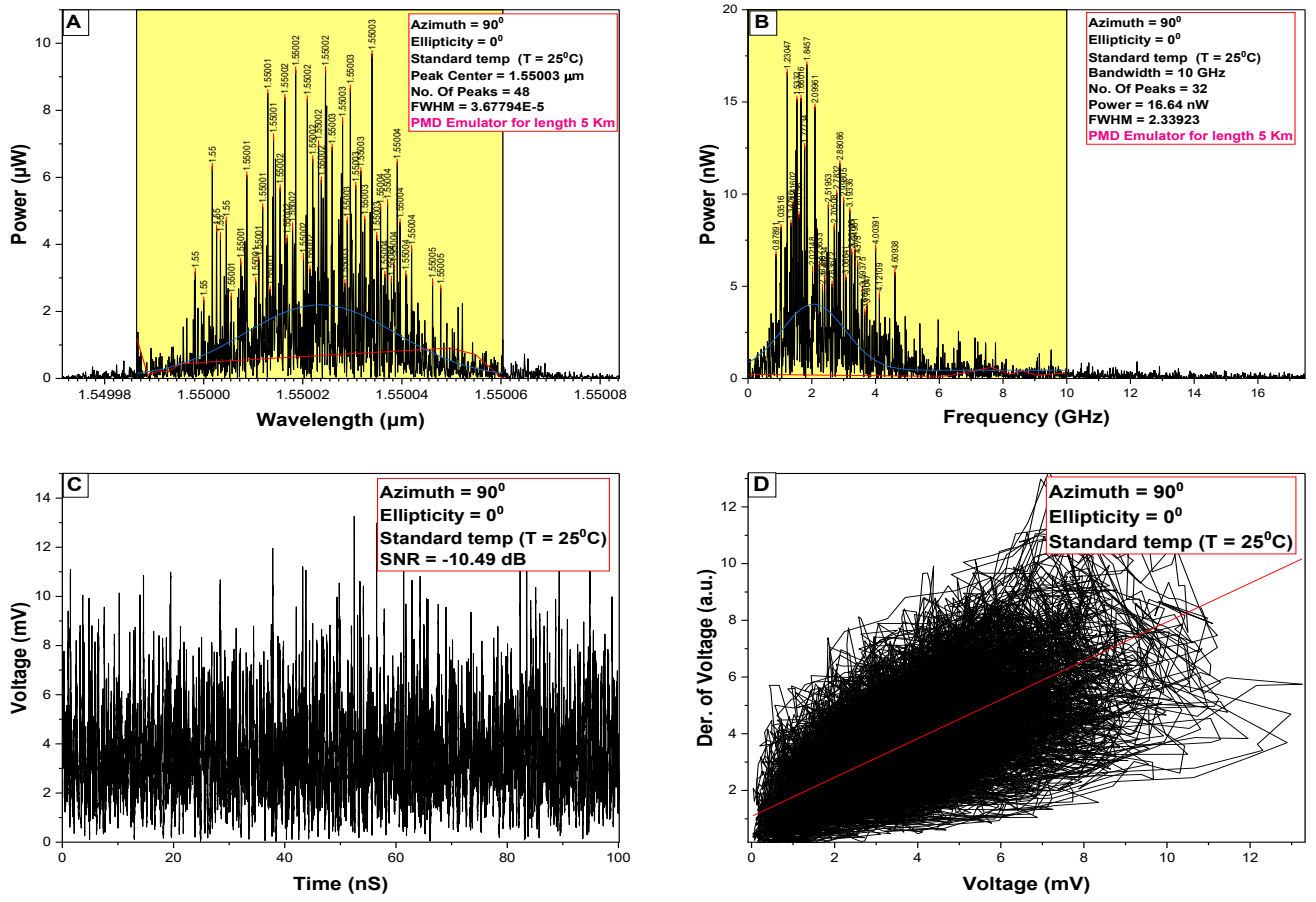

Fig. 7. Signal analysis after applying azimuth = 90° and ellipticity = 0°, L = 5 km. (A) Optical Spectrum, (B) The RF power spectra, (C) Time series, (D) The attractor (colour online)

The same procedure is resumed, altering the azimuth to 90° and subsequently to -90°, while maintaining the ellipticity constant at 0, consistent with prior instances. Observed results shown in Fig. 7A exhibit an unusual modification in dynamic behavior: the OSA presents a wider spectrum and an increased number of wavelengths, achieving 48 peaks, exceeding all other analyzed values for a fiber length of 5 km. The bandwidth extends to 10 GHz with 32 peaks, matching the chaotic behavior demonstrated by the RF at an azimuth of 45° and an ellipticity of 0°, as in Fig. 7B. Fig. 7C, changing the azimuth to 90° not only increases the BW and the number of peaks, but it also raises the frequency of the time series of chaotic oscillations by a large amount, reaching about 1129 peaks. The attractor's behavior indicates that its value persists in changing until its slope attains 0.68 (Fig. 7D).

A similar behavior is noted for (azimuth = -90° and ellipticity = 0°) as observed for (azimuth = -90°), although to a lower extent. Fig. 8A shows an expansion in chaotic dynamics and an increase in the frequency peak number with an increase in the value of the center frequency power P = 14 μW. On the other hand, the RF reveals no significant alterations in BW, the number of frequency peaks, or the power straight, as indicated in Fig. 8B. With about 827 frequency peaks recorded, the time series of chaotic oscillations behaves the same way at an azimuth of - 45° (Fig. 8C). Finally, it is observed that the attractor continuously decreases by a decimal fraction as the SOP changes, where the slope value is now 0.67, as shown in Fig. 8D.

The simulation is repeated by connecting two longer optical fibers, 10 and 15 km, as shown in Table 1.

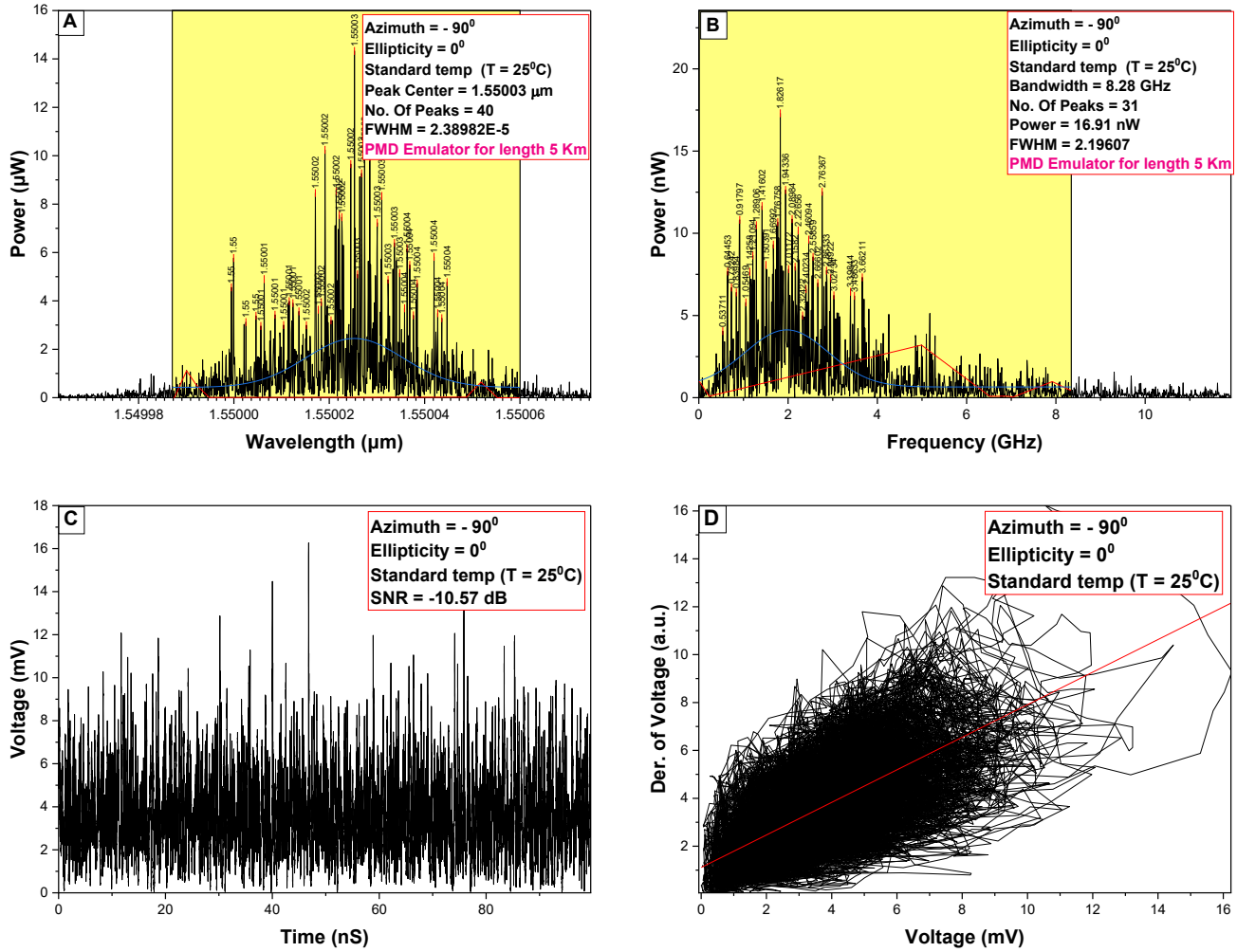

Fig. 8. Signal analysis after applying azimuth = -90° and ellipticity = 0°, L = 5 km. (A) Optical Spectrum, (B) The RF power spectra, (C) Time series, (D) The attractor (colour online)

Table 1. Statistics of measurements-based change in the SOP for the observed signals

		OSA			RF		
$\boldsymbol{\theta}$	Length km	No. of peaks	FWHM $\times 10^{-6}$	Center wavelength µm	No. of peaks	FWHM	Bandwidth GHz
(0,0)	10	39	3.855323	1.55002	20	1.41952	8.6
(45.0)	10	44	2.99789	1.55004	22	0.1785	7.18
(90,0)	10	44	3.93638	1.55003	23	0.14172	5.5
(-90.0)	10	42	3.29677	1.55001	27	1.91084	6.64
(0,0)	15	9	7.85631E-3	1.55	36	2.16905	7
(45,0)	15	30	1.12659	1.55	36	2.64146	5.5
(-45,0)	15	8	1.44814	1.55	34	2.57852	6.8
(90,0)	15	36	2.70583	1.55003	30	2.0093	8.2
(-90,0)	15	47	3.63865	1.55002	37	1.84014	8.6

The table presents the values of the number of peaks, FWHM, and BW of the spectrum captured from the OSA and RF after changing the length of the optical fiber and exposing it to the same circumstances experienced by the 5 km optical fiber. The results demonstrated a distinct interaction with variations in the length of the optical fiber regarding PMD, revealing that the intensity of observed signals is irregular. The BW of the resultant chaotic signal (L=10 km) reaches its maximum at 8.6 GHz with 20 peaks at azimuth = 0, while the minimum bandwidth occurs at azimuth = 90^o, (BW = 5.5) with 23 peaks for the signal obtained from the RF. For L=15 km, the maximum value of BW was observed at azimuth = -90^o, with 37 peaks in the spectrum gathered from the RF.

Additionally, it is noticed that an expansion is located in the width of the signal observed by the OSA spectrum. Also, the peak number jumps to 47 from just 9 peaks for the same spectrum at azimuth =0. The minimal bandwidth measured from the RF at an azimuth of 45 was BW = 5.5. Comparable to the expansion value in the chaotic dynamics of the spectrum at L = 10, but at a different azimuth. No substantial variation was observed in the number of peaks between the maximum and minimum values, which were measured at 36 and 37, respectively.

The final signal's chaotic behavior can be seen by examining the attractor and how it changes as the SOP is varied across the three optical fiber lengths. Fig. 9 shows a clear change in the expected behavior when the optical fiber is exposed to outside forces, like twisting, which changes the SOP. InvsPoly, GaussAmp, and Piecewise (PWL3) functions were applied as fitting functions to characterize the spectrum's shape.

Fig. 9A shows that the InvsPoly curve exhibits randomness and closely matches the spectrum's basic shape; furthermore, the InvsPoly fit yields an impressive R-squared (COD) enhancement and reduced error. The black curve demonstrates the original curve before the use of the fitting function, revealing rapid growth in the slope (the response of the attractor to variations in SOP) in the negative domain of the x-axis ($X < 0$), followed by a collapse in the positive domain ($X > 0$). The optimal fitting function for this description is InvsPoly, which is represented by the red curve. A flawless correspondence between the two curves cannot be assured, as the utilized fitting function cannot modify a minor linear behavior at certain points.

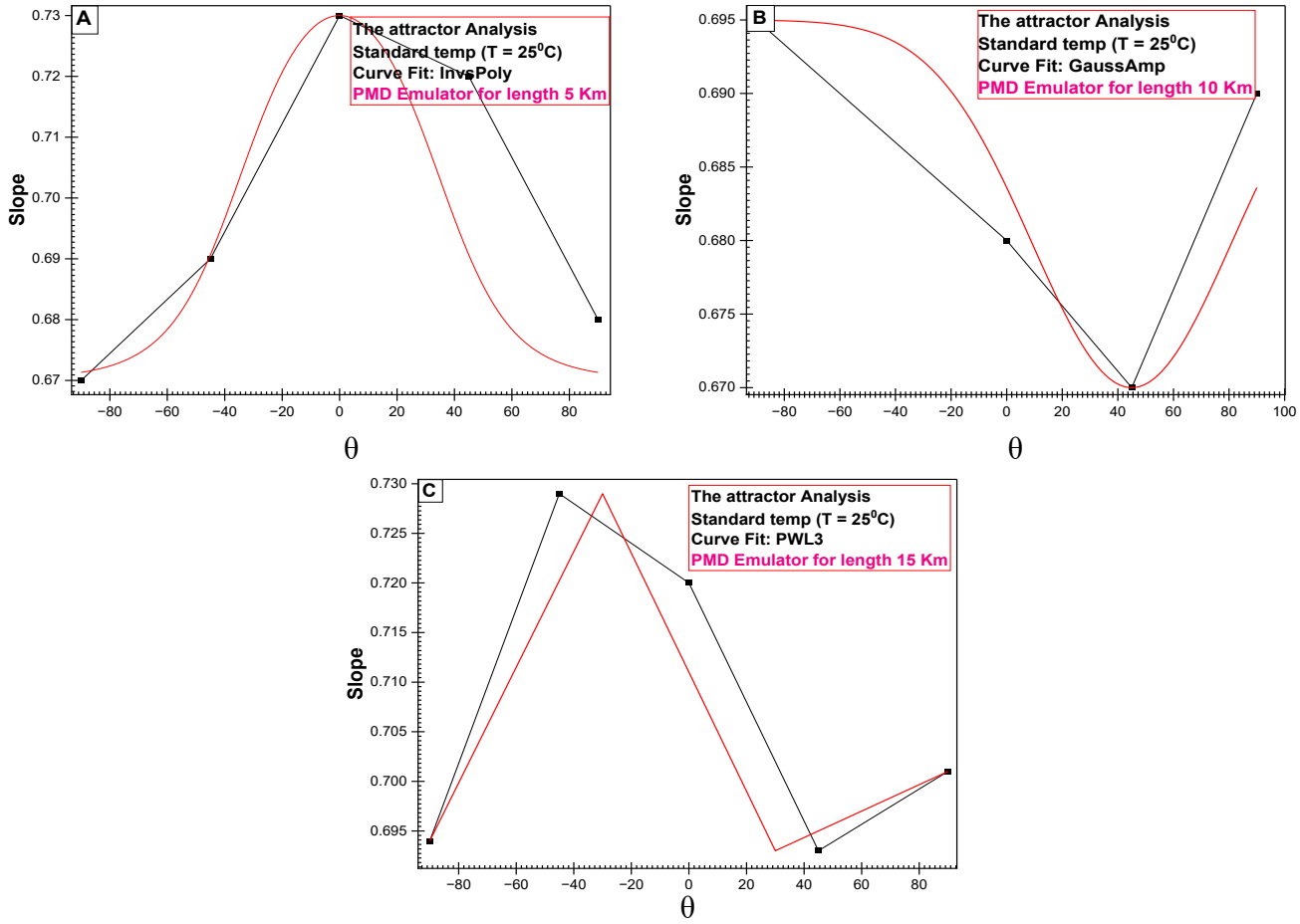

Fig. 9. The attractor analysis for DFB after the feedback injection for different optical fiber lengths. (A) L = 5 km, (B) L = 10 km, and (C) L = 15 km (colour online)

Fig. 9B illustrates the attractor's behavior concerning the variation in SOP; however, it is important to observe that the shape undergoes a major change when L=10 km. The fit of the GaussAmp function with the original curve indicates that the shift is symmetric, as this function represents a modified Gaussian model deployed to fit symmetric distributions. In the case of L=15 Km, the fitting (PWL3) function effectively describes the attractor's behavior corresponding to the angle obtained from the modification in SOP. This function is defined by approximating the nonlinear function (black curve) with a linear function divided into three linear segments, as illustrated in Fig. 9C. The first segment, indicated by (-90 to -30), exhibits an increase in the attractor's behavior at around azimuth = -90. A significant decline in behavior occurs in segment (-30 to 30) at an azimuth of -45 (segment two). The third segment (30 to 90), corresponding to the positive x-axis, reveals a modest increase in the attractor's behavior compared to the negative x-axis. This matches the findings from OSA and RF, which indicated that the chaotic fluctuation increases at an azimuth of 90°.

To characterize the complexity of the observed laser dynamics, we rely on the measurement of the Correlation Dimension (D_2) of the strange attractor, following the method proposed by Grassberger and Procaccia. This metric provides a lower bound to the fractal dimension of the attractor and is essential for distinguishing low-dimensional deterministic chaos from stochastic noise [35, 36]. If $D_2 = 0$ (fixed point) or $D_2 = 1$ (limit cycle) or $D_2 = 2$ (torus), then, deterministic chaos must occur within the range ($2 < D_2 < 3$), Consequently, a fractal dimension serves as an indicator of chaos [36]. All results from the study of the effect of detuning demonstrate deterministic chaos, as shown in the Table 2.

Table 2. Calculated correlation dimension

θ	Fiber Length (Km)	Embedding Dimension (m)	Correlation Dimension D_2
(0,0)	5	12	2.8158
(45.0)	5	12	2.5853
(-45.0)	5	12	2.8516
(90,0)	5	12	2.6058
(-90.0)	5	12	3.1564

An indirect method has been used to determine the feedback level, depending on the evaluation of feedback effects on the threshold of laser-stimulated emission. As reported by ref. [37], when the edge-emitting diode device

with a Fabry-Perot cavity type is subjected to optical feedback, the threshold decreases linearly with the feedback rate, resulting in the reinjected backlight beam into the laser cavity being compared to a proportional increase in laser gain. Simulation observations agree with the last reported relation, even though the simulated laser source is a DFB-type cavity, such that it is noted that the threshold reduction of DFB also decreases linearly, which increases the power efficiency of DFB.

Fig. 10A demonstrates how the number of peak variations leads to asymmetric saddles due to variation attained against several SOP values. This contrasts with the results of VCSEL lasers, which typically exhibit near symmetry, as indicated in ref. [38]. The figure indicates that modifying the SOP leads to periodic fluctuations in the number of peaks, reaching a maximum at an azimuth of 90°, thereby verifying the interaction between the feedback signal and the frequencies within the laser cavity.

Fig. 10B illustrates the effect of the FWHM measured by the OSA, showing the same periodic behavior as the SOP is varied at an azimuth of 45°. Fig. 10C demonstrates the correlation between the variation of SOP and the number of peaks according to the RF analysis, distinguished by the piecewise PWL2 function, which indicates a rapidly increased frequency until a maximum value, followed by a rapid decrease in the frequencies for the same dynamics. Radio frequency analysis shows that the FWHM value fluctuates with SOP, matching the periodic behavior seen by OSA as shown in Fig. 10D. The BW tends to correspond with the linear relationship represented by the piecewise function PWL2, as illustrated in Fig. 10E, which exhibits a linear increase, reaching the highest value of chaotic dynamics at an azimuth of 90° and a BW of 10 GHz.

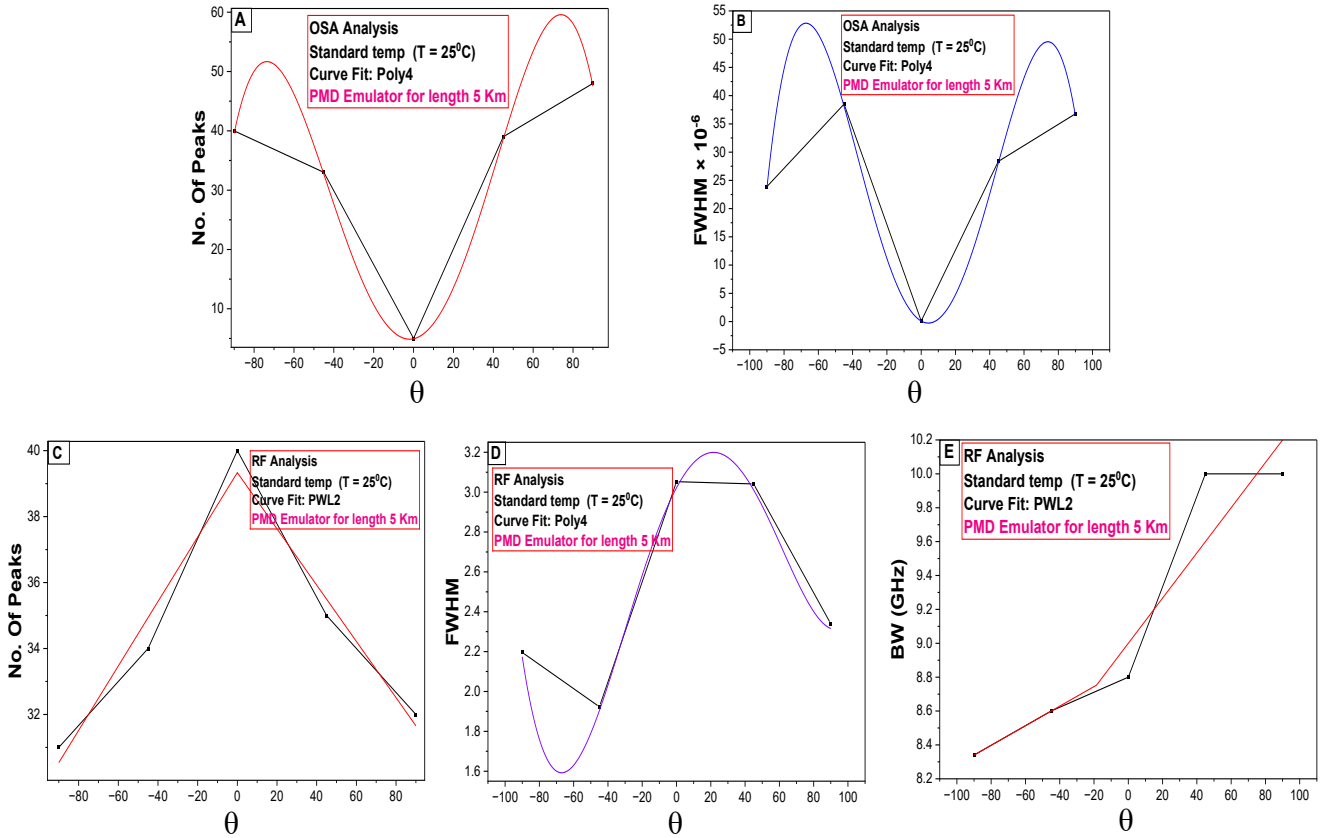

Fig. 10. Statistics of signal dynamics observed with 5 km PMD fiber length against SOP. (A&B) represent the No. of peaks and FWHM of optical spectrum analyser (OSA), (C) & (D) & (E) represent the No. of peaks, FWHM & BW of RF analyser (colour online)

The quantity of DGD is known to fluctuate in direct proportion to the length of the optical fiber, as shown by the equation [32]:

$$DGD = DGD_{Cof} \times \sqrt{L} \tag{12}$$

where DGD_{Cof} is the PMD coefficient, which has a standard value of 10.04 $ps/\sqrt{Km}$ based on the simulation executed in OptiSystem. Every modification in the length of the optical fiber leads to an associated variation in the DGD value, as seen by the increase in optical fiber length to 10 and 15 km, as illustrated in Table 3.

Table 3. DGD values per optical fiber length

Fiber Length (Km)	DGD ($ps/\sqrt{Km}$)
5	22.5
10	31.8
15	38.88

A high DGD value may lead to unpredictable changes in the polarization state, which can destabilize the laser and cause chaotic variations in bandwidth, number of peaks, and FWHM. This irregularity was observed when varying the length of the optical fiber, as shown in Figs. 11 & 12.

In the last two Figs. 11A and 12A, the fitting of the resulting no. of peaks becomes bi-Gaussian & Poly4, respectively, compared with 5 km in Fig. 10A, indicating the development of laser dynamics.

Polynomial functions, such as Poly4, exhibit symmetrical behavior based on the parity of the function's value, whether odd or even. The graph is symmetrical about the $y-axis$, That is, $f(-x)=f(x)$. But if the function is odd, then the graph becomes symmetrical about the origin, that is, $f(-x)=-f(x)$. Nonetheless, the figures (11A and 12A) do not satisfy this requirement, confirming the asymmetrical behavior of chaotic dynamics. The same development is observed when figures (11B and 12B) are compared with Fig. 10B, where fitting is transformed from the (Poly4) function to the (PWL3) function in Fig. 11B, while it shares the same (Poly4) fitting function with Fig. 12B.

For L = 10 Km, Fig. 11B shows chaos characteristics in response to the fluctuation in SOP. The fitting function PWL3 estimates the nonlinear function (black curve) as a linear function divided into three linear segments. The first segment, described by the negative angle region, it is observed that the FWHM value increases smoothly compared to the rapid increase of the FWHM for (L = 5 km) shown in Fig. 10B. A noticeable reduction in behavior is evident in the segment (-30 to 30) at azimuth -45, however, a bit smaller than the gradient observed at (L = 5 km). The third segment (30 to 90) exhibits a more significant rise in chaotic behavior than the negative angle region.

Fig. 12B demonstrates the correlation between FWHM and SOP at (L = 15 Km). It is exciting that the fitting function employed is similar to that used at (L = 5 km), particularly the Poly4 function, which yields the same asymmetry previously observed. Figs. 11C & 12C exhibit the relation between the fluctuations of SOP and BW given by the RF analysis, defined by the nonlinear PWL2 and Cubic functions, respectively. PWL2 in Fig. 11C behaves similarly to the previously mentioned fitting function (PWL3), but it approximates the nonlinear function to be linear by segmenting it into two regions rather than three. The change for negative azimuth angles is greater than that caused by positive azimuth angles.

In Fig. 12C, a (cubic) function was used, which is one of the types of polynomial functions. It is observed from the behavior of this function that it is also a case of asymmetry, because the coefficient of $X^2, (b \neq 0)$.

Comparing Fig. 11D with Fig. 10D, it can be noticed that the cubic function has been chosen as the appropriate fitting function to characterize the relation between FWHM and SOP, indicating that chaotic behavior at (L=10 Km) occurs frequently in the negative azimuth region, aligning with previous cases. As for Fig. 12D, it is observed that the fitting function (Poly4) is used to describe the chaotic behavior. Although the various fitting functions that describe the relationship between BW and SOP in each of the three cases (L = 5, 10, 15) Km, they all exhibit an unpredictable chaotic behavior of rapid growth followed by rapid decline Figs. 11E & 12E.

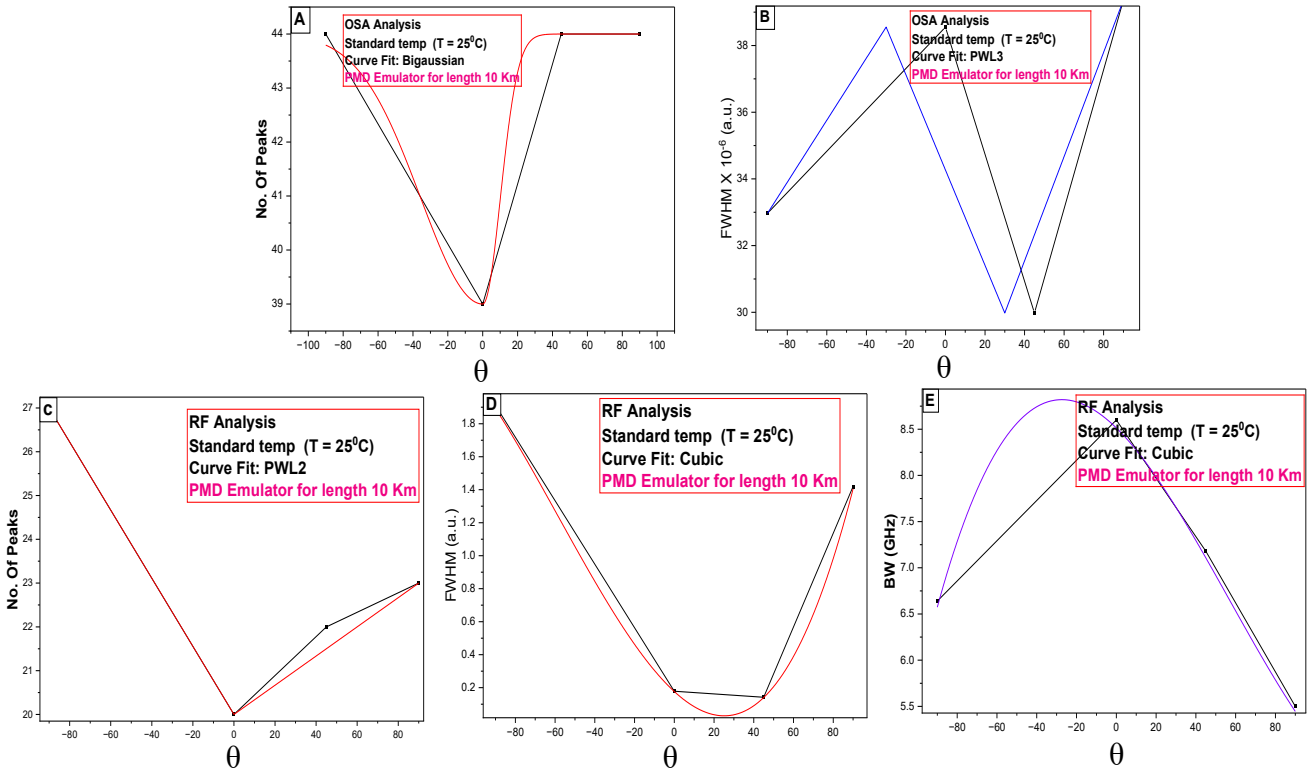

Fig. 11. Analysis of signal dynamics observed with 10 km PMD fiber length against SOP. (A&B) represent the No. of peaks and FWHM of optical spectrum analyser (OSA), (C) & (D) & (E) represent the No. of peaks, FWHM & BW of RF analyser (colour online)

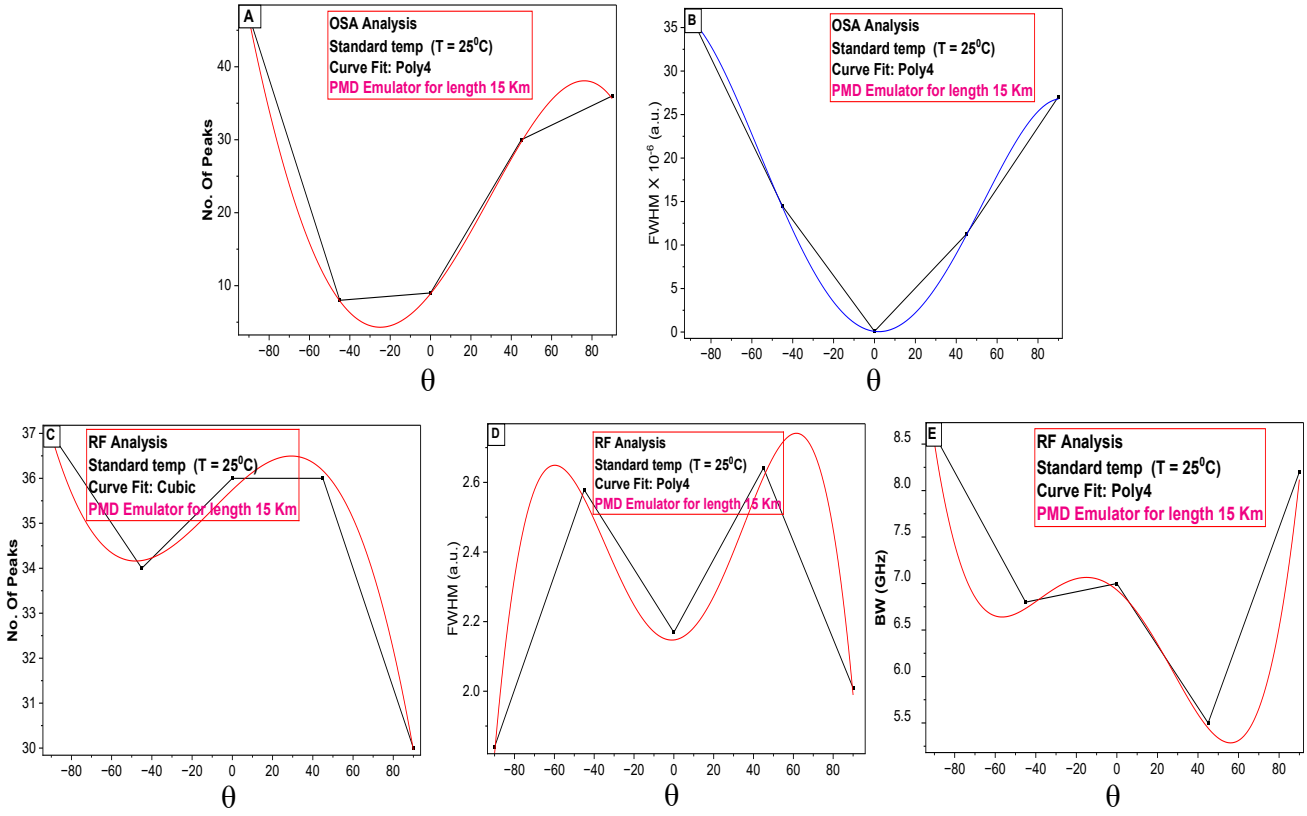

Fig. 12. Analysis of signal dynamics observed with 15 km PMD fiber length against SOP. (A&B) represent the No. of peaks and FWHM of optical spectrum analyser (OSA), (C) & (D) & (E) represent the No. of peaks, FWHM & BW of RF analyser (colour online)

5. Conclusions

Results presented a study of the SM effect on LD using the PC to generate the change in the SOP and the PMD emulator to generate the DGD. A simulation study is made to enhance the chaotic behavior of the DFB. The results showed that the signal amplitude fluctuates and does not exhibit a periodic form, but rather varies with time when the SOP is changed, acting as an external disturbance. This happens because DGD, caused by PMD, splits the two polarization components and makes them travel at different speeds, leading to birefringence. RF spectrum measurements showed a wide range of frequencies in the laser spectrum due to interference between modes in the DFB cavity and the signal reflected from the PMD, indicating that the system has reached relaxation oscillations and a state of artificial disorder.

Acknowledgements

The authors would like to thank Mustansiriyah University, Baghdad- Iraq for their support of this research.

References

[1] M. Jaber, A. A. Hemed, Mustansiriyah Journal of Pure and Applied Sciences **3**(4), 117 (2025).
[2] D. R. Madhloom, A. A. Hemed, S. M. Khorsheed, East European Journal of Physics **2**, 267 (2023).
[3] R. Zhang, P. Zhou, Y. Yang, Q. Fang, P. Mu, N. Li, Opt. Express **28**(5), 7197 (2020).
[4] Y. Doumbia, T. Malica, D. Wolfersberger, M. Sciamanna, Opt. Lett. **48**(6), 1442 (2023).
[5] T. R. Raddo, K. Panajotov, B. H. V. Borges, M. Virte, Sci. Rep. **7**(1), article number: 1598 (2017).
[6] Z. R. Ghayib, A. A. Hemed, Pramana **96**(2), 86 (2022).
[7] H. Bian, X. Zhang, P. Li, Zhiwei Jia, Li Ma, Bingjie Xu, Keith Alan Shore, Yuwen Qin, Yuncai Wang Photonics **10**(2), 219 (2023).
[8] A. A. Hemed, T. Ackemann, H. J. Kbashi, B. T. Chead, Journal of Physics: Conference Series **1818**(1), article number 012027 (2021).
[9] K. Schires, S. Gomez, A. Gallet, G. H. Duan, F. Grillot, IEEE Journal of Selected Topics in Quantum Electronics **23**(6), 1 (2017).
[10] X. Mu, Z. Yan, Y. Yu, H. Yan, D. Han, Opt. Laser Technol. **127**, 106172 (2020).
[11] M. Chai, Lijun Qiao, Xiaojing Wei, Shuhui Li, Chenyang Zhang, Qin Wang, Henry Xu, Mingjiang Zhang, Opt. Express **30**(25), 44717 (2022).
[12] H. Han, M. J. Zhang, K. A. Shore, IEEE Journal of Quantum Electronics **55**(3), 1 (2019).
[13] A. A. Hemed, R. S. Abbas, Current Overview on Science and Technology Research **8**, B P International

120 (2022).
[14] Ayser A. Hemed, Mustansiriyah Journal for Sciences and Education **17**(1), 77 (2016).
[15] Z. Liu, R. Slavik, Journal of Lightwave Technology **38**(1), 43 (2020).
[16] H. H. Khalaf, A. A. Hemed, Journal of Optics (2025), doi: 10.1007/s12596-025-02509-w.
[17] N. M. Al-Hosiny, International Journal of Optics **2024**, 1 (2024).
[18] Ayser A. Hemed, "Studying the effective factors on producing model birefringence (high and low) in the single-mode optical fiber," M. Sc. Thesis, Mustansiriyah University, Baghdad, 2005.
[19] K. Perlicki, 'Polarization Effects in Optical Fiber Links', in: Advances in Optical Fiber Technology: Fundamental Optical Phenomena and Applications, Edited by Moh Yasin, H. Arof, S. W. Harun, InTech, 2015.
[20] L. L. Fan, Y. Li, J. Li, Y. Hao, H. Ren, S. Cao, S. Liu, Weijie Ding, Juanfen Wang, Lingzhen Yang, Results in Physics **63**, 107866 (2024).
[21] R. Khosravani, I. T. Lima, Jr., P. Ebrahimi, E. Ibragimov, A. E. Willner, C. R. Menyuk, IEEE Photonics Technology Letters **13**(2), 127 (2001).
[22] S. Ten, "An Introduction to the Fundamentals of PMD in Fibers Introduction: Importance of PMD for High Data Rate Transmission Systems." [Online]. Available: https://www.researchgate.net/publication/242534239.
[23] Petr Drexler, Pavel Fiala, "Optical Fiber Birefringence Effects – Sources, Utilization and Methods of Suppression," in Recent Progress in Optical Fiber Research, Edited by Moh Yasin, S. W. Harun, H. Arof, Rijeka, Croatia: IntechOpen, ch. 7, pp. 128–150, 2012.
[24] R. Shafin, P. Sen, S. Basak, A. Islam, S. P. Majumder, M. S. Islam, 2012 7th International Conference on Electrical and Computer Engineering 43 (2012).
[25] J. Jason, P. Rugeland, O. Tarasenko, W. Margulis, H.-E. Nilsson, Applied Optics **52**(21), 5208 (2013).
[26] G. Agrawal, Nonlinear Fiber Optics, Fifth Edition, Elsevier, 2013.
[27] R. Lang, K. Kobayashi, IEEE Journal of Quantum Electronics **16**(3), 347 (1980).
[28] G. Acket, D. Lenstra, A. Den Boef, B. Verbeek, IEEE Journal of Quantum Electronics **20**(10), 1163 (1984).
[29] G. Giuliani, M. Norgia, S. Donati, T. Bosch, Journal of Optics A: Pure and Applied Optics **4**(6), S283 (2002).
[30] W. M. Wang, K. T. V. Grattan, A. W. Palmer, W. J. O. Boyle, Journal of Lightwave Technology **12**(9), 1577 (1994).
[31] F. Treviño-Martínez, D. Tentori, C. Ayala-Díaz, F. J. Mendieta-Jiménez, Opt. Express **13**, 2556 (2005).
[32] N. Malhotra, M. Kumar, Optik **121**(3), 286 (2010).
[33] R. Kieser, P. Reynisson, T. J. Mulligan, ICES Journal of Marine Science **62**(1), 123 (2005).
[34] C. Grebogi, E. Ott, J. A. Yorke, Science **238**(4827), 632 (1987).
[35] P. Grassberger, I. Procaccia, Physica D: Nonlinear Phenomena **9**(1-2), 189 (1983).
[36] F. T. Arecchi, R. G. Harrison (Eds.) "Instabilities and chaos in quantum optics" (Springer Series in Synergetics; Vol. 34). Springer, 1987
[37] Ayser A. Hemed, "Chaos Generation Methods in Optical Communication Systems," Ph. D. Thesis, University of Baghdad, Baghdad, 2011.
[38] Y. Hong, P. S. Spencer, K. A. Shore, J. Opt. Soc. Am. B **29**, 415 (2012).

*Corresponding author: ayser.hemed@uomustansiriyah.edu.iq